Nacelle Design for Ultra-High Bypass Ratio Engines with CFD Based Optimisation

Matthew Robinson, David G MacManus, Robert Christie, Christopher Sheaf, Nicholas Grech

PII: S1270-9638(20)30873-7
DOI: https://doi.org/10.1016/j.ast.2020.106191
Reference: AESCTE 106191

To appear in: *Aerospace Science and Technology*

Received date: 16 July 2018
Revised date: 1 March 2020
Accepted date: 3 September 2020

Please cite this article as: M. Robinson et al., Nacelle Design for Ultra-High Bypass Ratio Engines with CFD Based Optimisation, *Aerosp. Sci. Technol.* (2020), 0, 106191, doi: https://doi.org/10.1016/j.ast.2020.106191.

Aerospace Science and Technology, Volume 113, June 2020, Article number 106191
DOI:10.1016/j.ast.2020.106191

Nacelle Design for Ultra-High Bypass Ratio Engines with CFD Based Optimisation

Matthew Robinson[a], David G MacManus[a,*], Robert Christie[a], Christopher Sheaf[b], Nicholas Grech[b]

[a] *Centre for Propulsion Engineering, School of Aerospace, Transport and Manufacturing, Cranfield University, Bedfordshire, MK43 0AL*
[b] *Rolls-Royce plc., P.O. box 31, Derby, United Kingdom, DE24 8BJ*

Abstract

As the size of aero-engines has increased in recent years, the need for slimmer and shorter nacelles has become more pressing. A more aggressive design space must therefore be explored for nacelle designs which are expected to perform worse in the off design conditions such as spillage than current nacelle designs. In this work, a novel design space has been explored through the use of an optimisation method which evaluated nacelle aerodynamic performance based on computational fluid dynamics simulations. A multi-objective optimisation was undertaken where cruise drag, drag rise Mach number, spillage drag and two metrics based on the pressure distribution of the nacelle were optimised. Comparable optimal designs were picked from the Pareto sets of optimisations carried out at different nacelle lengths and radial offsets and some key outcomes established from their aerodynamics and geometries. It was determined that a reduction in the length of the nacelle from 3.8 highlight radii to 3.1 radii resulted in a significantly worse aerodynamic performance which included an increase in peak surface isentropic Mach number at cruise of 0.1 and up to four times as much spillage drag. It was however also established from the optimisation results that as the required drag rise Mach number was decreased the overall performance of short nacelles improved significantly.

Keywords: Optimisation; Nacelle; CFD; UHBPR.

Nomenclature

Roman Symbols

A	Area
$C_{Dcruise}$	Nacelle drag evaluated at cruise point
C_{Dnac}	Nacelle drag
C_{Dspill}	Nacelle drag evaluated between end of cruise and mid cruise
f	Non-dimensional factor
m	Number of objectives
r	Radius
C	Class function
D	Drag
h	Altitude
i	Index of summation
K	Binomial coefficient
k	Order of derivative
M	Mach Number
N	Upper bound on summation

*Corresponding author.
E-mail address: d.g.macmanus@cranfield.ac.uk

N_1 First exponent in the class function

N_2 Second exponent in the class function

S Shape function

x Abscissa

Greek Symbols

β Boat-tail angle

κ Curvature

λ Second derivative of c_p at a change of polarity of c_p gradient

ϕ Force

ψ Non-dimensional abscissa

ξ Non-dimensional ordinate

Superscripts and Subscripts

∞ Freestream

fb Forebody

hi Highlight

if Initial Forebody

max Maximum radius

nac Nacelle

$post$ Post-exit

pre Pre-entry

TE	Trailing Edge
0	Upstream infinity plane
1	Highlight plane
bp	Bernstein polynomial weighting coefficient
DR	Drag Rise

Acronyms

BPR	Bypass Ratio
CFD	Computational Fluid Dynamics
iCST	Intuitive Class/Shape Transformation
MFCR	Mass Flow Capture Ratio
MOO	Multi-objective optimisation
NSGA-II	Non-dominated Sorting Genetic Algorithm II
RANS	Reynolds Averaged Navier Stokes
SST	Shear Stress Transport

1. Introduction

As the bypass ratio (BPR) of turbofan engines increases [1] the fan diameter generally also increases. This will incur additional nacelle weight and drag penalties and, as such, the nacelle design becomes more important. Performance penalties from heavier nacelles with more drag may ultimately outweigh the efficiencies gained from the engine cycle and hence designers will aim for increasingly short and slim fan cowls [2][3]. There has been a resultant effort to

understand the aerodynamics of nacelles and provide improved solutions for future engines[4, 5, 6]. A 'slimline' nacelle is expected to be incorporated in future, large engine designs [5] however the aerodynamic performance of these designs may be a limitation, particularly at off design conditions or when installed in the pressure field around an aircraft wing [7]. Historically, an aero-engine nacelle was designed from aerofoil shapes revolved around an engine axis chiefly defined by the leading edge (highlight) radius, maximum radius and a curvature profile [8]. A conventional nacelle design in cruise will typically incorporate a curvature driven acceleration, which peaks on the forebody, followed by a constant deceleration [9]. For nacelles which operate in the transonic regime the acceleration will produce a sonic region and a shock wave which will incur drag penalties. To design a nacelle which has decreased maximum diameter it will be necessary to increase the external lip curvature which will increase the peak acceleration. This will result in greater wave drag and a nacelle which may offset the installed engine efficiency gained from the greater fan diameter. For example, a study of nacelle aerodynamics [10] demonstrated that shortened nacelles may exhibit non-monotonic velocity profiles and high peak Mach numbers in cruise flight. Furthermore, the same study demonstrated that a reduction in length from $L_{nac}/D_{fan} = 2.5$ to $L_{nac}/D_{fan} = 0.6$ resulted in a threefold increase in the drag at freestream Mach $M_\infty = 0.8$ and at 10668m altitude.

In addition to the cruise portion of the flight, a nacelle must be optimised for several off design conditions which are encountered throughout a typical mission profile. For example, whilst the design point of an engine might be at a mid-cruise condition, throughout the cruise the aircraft weight decreases and therefore the thrust is adjusted for the re-trimmed aircraft. As a result of this, the mass flow through the engine will decrease. This decreased mass flow results in a lower mass flow capture ratio, $MFCR = A_0/A_1$. The MFCR describes the

streamtube which enters the engine (Figure 1) where A_0 is the cross sectional area of the streamtube at the upstream infinity plane and A_1 is the area of the highlight. A lower value means that the local incidence at the lip of the nacelle increases since the streamtube area change is greater. In the later stages of the cruise, the nacelle design becomes more critical as the forebody suction must increase to balance the change in momentum of the streamtube. Any imbalance between these two forces is called spillage and the nacelle drag increases [11]. A decrease in the MFCR can result in higher peak Mach numbers encountered on the cowl which can incur greater wave drag and losses. The drag rise Mach number is another important performance indicator which indicates the onset of large amounts of wave drag due to the compressibility of the airflow. At certain points in the flight envelope it may be necessary for the aircraft to operate at higher Mach numbers. It is therefore important to ensure that the nacelle is not close to the transonic boundary at which the drag will diverge. It is also important to consider that interference effects between the engine, designed in isolation, and the airframe may result in higher local accelerations than were present in isolation. A margin of safety is therefore introduced between the design point and the drag rise Mach number (also known as the drag divergence Mach number) of the nacelle [12]. Knowledge of the drag rise Mach number is therefore important in preliminary design. Since the nacelle must operate across a range of conditions it is important to ensure that there are not unacceptable levels of drag at off design with different freestream Mach numbers and mass flows. The aerodynamic design of the fan cowl must also be compatible with the remainder of the nacelle requirements. For instance, the nozzle geometry is designed to deliver a particular mass flow and therefore prescribes an exit area which the trailing edge of the fan cowl must be compatible with. In addition, the nacelle housing needs to include some engine structure and components

which would dictate a minimum outer radius of the fan cowl. Finally, it is vital to ensure the engine can be successfully integrated with the aircraft and the requirements for a suitable installation will also manifest in the nacelle design.[13]

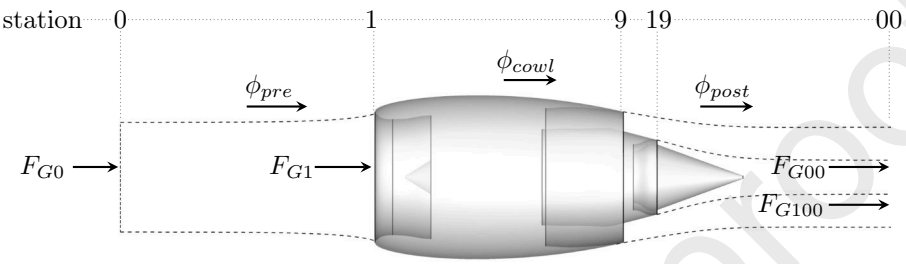

Figure 1: Thrust and drag accounting system

Due to the multiple off design conditions which must be simultaneously satisfied it is difficult to design a short nacelle which performs adequately in terms of the aerodynamic characteristics [10]. The multiple requirements which must be simultaneously met make this problem ideal for multi-objective optimisation (MOO). There are many algorithms capable of simultaneously optimising two or more objectives. One set of algorithms involve treating the input variables as genes and the output variables as phenotypic characteristics analogous with evolutionary theory. These genetic algorithms create populations of individuals which are evaluated against each other based on tournaments of their fitness. This fitness is determined as a function of the objective values which are to be optimised and subsequent generations are produced as offspring of the best individuals. This process is repeated for a given number of generations of individuals and the outcome should be an approximation of the Pareto set which describes an m-dimensional surface of the optimal individuals which can be achieved for the given objective functions. Genetic algorithms have previously been applied to a number of MOO aerodynamic problems [14] [15] and have shown a capabil-

ity to simultaneously optimise at several aerodynamic points. Previous studies have also been carried out specifically on the problem of nacelle external design through optimisation [16, 17, 18, 19, 20]. Two of these studies [17] [18] focussed on the use of a surrogate model to provide a quicker optimisation approach. Both of these studies used a CFD method to obtain high fidelity simulations of the nacelles which were used to improve a surrogate model. This resulted in improvements from a baseline design but since they did not simulate multiple points in the CFD model they could not directly assess the suitability of the designs at off design conditions. Since this is expected to be a major challenge for future high BPR engines, this is a gap which the present study aims to fill. The studies also did not focus on high transonic Mach number operations and as such the expected problems of off design would have been lessened. As computational fluid dynamics (CFD) approaches become more computationally efficient and resource more readily available a direct CFD optimisation approach becomes possible. One study which used direct CFD simulation [16] demonstrated the applicability of multi-objective optimisation to isolated nacelles. In this study the focus was on cruise and cross-wind performance and produced a Pareto front of pressure drag and intake distortion. The authors concluded that whilst the Pareto front was established further constraints were required to avoid unrealistic shapes. For example, the optimal fan cowl produced for the two objectives demonstrated two peaks in negative pressure coefficient which were more severe than the baseline. This would result in increased spillage as it strengthens the shock wave at lower MFCRs. Another multi-objective optimisation study of nacelles [19] minimised fan cowl peak Mach number during cruise and intake peak Mach number in a take-off condition. This study did not directly consider the drag performance in cruise however and also did not look at spillage or drag rise.

The aim of this paper is to demonstrate a method of genetic optimisation for transonic nacelle design with typical multi-objective requirements which encompass design and off-design conditions. The method is then applied to short and slim nacelles for large, low specific thrust engines to determine the design space for future turbofans. The research applies a multi-objective genetic algorithm based on CFD simulations to a novel region of the design space and develops the method to assess these designs.

2. Methodology

2.1. Engine geometric definition and cycle model

Class shape transformation (CST) curves have been shown to create aerodynamically useful shapes for wing, nacelle and intake design [21, 22, 23, 24]. This method can be applied to create shapes with a relatively small number of input variables [21]. A CST curve is formed by the product of a Class Function, $C(\psi)$, and a Shape Function, $S(\psi)$ (equation 1). The Class Function defines the basic aerodynamic shape (equation 2). An additional term, $(\psi\Delta\xi_{te})$, is included to modify the end point's ordinate [21]. The inherent mathematically smooth behavior of Bernstein polynomial shape functions and the associated curvature continuity make this system ideal for aerodynamic design.

$$\xi(\psi) = S(\psi)C(\psi) + \psi\Delta\xi_{TE} \;\; ; \;\; \xi = \frac{y}{c} \;\; , \;\; \psi = \frac{x}{c} \tag{1}$$

$$C_{N_2}^{N_1}(\psi) = \psi^{N_1}[1-\psi]^{N_2} \;\; for \;\; 0 \leq \psi \leq 1 \tag{2}$$

However, one drawback of the CST approach is that the shape is controlled via a set of coefficients which are non-intuitive to the aerodynamic designer. For a specific set of constraints this drawback had been addressed by combining the

intuitiveness of the parameterisation method for airfoil sections (PARSEC) [25] with the highly flexible CST parameterisation method [26]. This intuitive CST (iCST) approach maps the CST coefficients to a full set of intuitive parameters through a transformation matrix [26]. The iCST approach has been generalised so that the transformation matrix which allows a CST parameterised fan cowl and intake to be fully defined by aerodynamically intuitive design variables which can be calculated analytically [27]. In this generalised iCST approach [27] an arbitrary number of constraints (N_{con}) such as position, gradient, and derivatives up to the n^{th} degree can be specified. A linear set of equations can be constructed from equation 3 and the magnitude, $\xi^{(k)}$, and abscissa, ψ of each constraint. The shape function and its derivatives can be solved by using the fact that derivatives of the k^{th} degree Bernstein polynomials are polynomials of degree $k-1$ and can be written as a linear combination of Bernstein polynomials (equation 4) [27]. This linear set of equations, or transformation matrix, can then be solved for the Bernstein polynomial coefficients.

$$\xi^{(k)}(\psi) = \left[\sum_{i=0}^{N}\left[bp_i K_{i,n}\left(\psi^i\left(1-\psi\right)^{n-1}\right)\right]C(\psi) + \psi\Delta\xi_{te}\right]^{(k)} \tag{3}$$

$$\frac{d}{d\psi}BP_{i,n}(\psi) = n[BP_{k-1,n-1}(\psi) - BP_{k,n-1}(\psi)] \tag{4}$$

A definition for engine nacelles has been established which allows for a series of aerolines which describe the intake, fan cowl, bypass stream duct, core stream duct, plug and spinner to be defined by a small number of intuitive design parameters (Figure 2) [28]. In this parameterisation, each aeroline is defined by a single intuitive class shape transformation (iCST) [26] [29] curve with the exception of the fan cowl which is defined by two curves. One previous study of multi-objective nacelle optimisation [19] concluded that a class-shape

transformation parameterisation converged to better designs than a comparable B-spline or superellipse polynomial parameterisation in terms of peak Mach number. These curves represent the fan cowl forebody and fan cowl afterbody separately and are joined at the position of maximum radius. At this position the two curves are constrained to have the same position, first derivative, and second derivative, hence ensuring curvature continuity. A bypass duct, core duct and plug geometry was determined for a baseline geometry to have the correct mass flows required by the cycle at the design point with an existing geometry definition tool, GEMINI [30]. GEMINI can create a representative axisymmetric definition of an aero-engine geometry which includes a bypass duct, core duct, core cowl and plug which are sized for a required engine mass flow and pressure ratios. This nozzle geometry was then fixed for all designs and translated, when required, to match a given trailing edge radius (r_{TE}). Five variables were chosen to be varied in the fan cowl optimisation [β, r_{max}, l_{fb}, r_{if}, y''_{TE}] (Figure 2), with y''_{TE} representing the second derivative at the trailing edge of the fan cowl. These parameters were chosen to give a suitable level of control over both the size and shape of the nacelle. The highlight radius (r_{hi}) (Figure 2) is common with the intake and, as discussed, determines the mass flow capture ratio for the fan cowl. The initial forebody radius (r_{if}) is the inverse of the curvature at the cowl lip. A high value will therefore indicate less curvature and a more blunt fan cowl. The maximum radius (r_{max}) and length (l_{nac}) are usually determined together to ensure space within the nacelle for all the engine sub-systems and the thrust reverse unit. In addition, these two parameters have a direct importance to the aerodynamics since they determine the fineness of the fan cowl. In general, it is desirable to minimise the maximum radius and the length to reduce the profile drag of the fan cowl. The r_{max} chosen for a design also has fundamental implications to the installation interference

on the aircraft wing due to close coupling and ground clearance. The axial position of the maximum radius (l_{fb}) (Figure 2) determines the split between forebody and afterbody. The trailing edge radius (r_{TE}) is largely fixed by the requirements of the engine nozzle exit area and the core cowl size. The fan cowl boattail angle (β) also needs to be compatible with the angles of the core cowl and plug whilst being small enough to avoid a diffusive separation or excessive boundary layer growth on the afterbody of the fan cowl. The curvature at the trailing edge is controlled by the specification of the second derivative (y''_{TE}) here. Combined with the boattail angle, which implicitly sets the gradient, this gives a control over the curvature directly since $\kappa = y''/(1 + y'^2)^{\frac{3}{2}}$. A fan cowl must ultimately be a trade off of performance at different conditions determined by the combination of these input variables. For instance, whilst cruise performance may favour a higher r_{if}, the higher cruise Mach operation would not. The determination of this trade off, mathematically stated, is a multiple objective optimisation problem. For each of these variables, a bounded region of interest was determined for the simulations of different geometries in this paper (Table 1). For the forebody length, initial forebody radius and maximum radius were bounded in their non-dimensionalised form (Table 1). To simulate the flow through the engine, an engine cycle was created which represented a two-spool geared turbofan designed to operate at $M_\infty = 0.85$. This was modelled in Turbomatch [31], a zero-dimensional engine modelling tool. The model provided aerodynamic boundary conditions for a series of points within the engine flight envelope which could be used for the CFD analyses.

Variable	Lower Bound	Upper Bound
β	11.0°	14.0°
r_{max}/r_{hi}	1.08	1.4
$f_{max} = l_{fb}/l_{nac}$	0.2	0.5
y''_{TE}	-0.5	0.5
$f_{if} = r_{if} l_{fb}/(r_{max} - r_{hi})^2$	0.6	1.35

Table 1: Optimisation bounds for nacelle geometric parameters

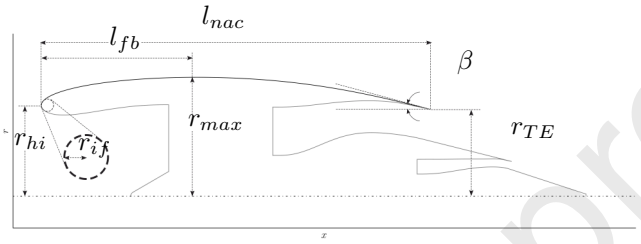

Figure 2: Geometric parameterisation of nacelle

2.2. Optimisation method

A real-parameter optimisation routine was developed based on the non-dominated sorting genetic (NSGA-II) algorithm [32]. Real-parameter coding was used as opposed to binary coding to avoid problems such as Hamming cliffs which can exist when the fitness values are treated as binary strings [32]. The generational optimisation method ranks a set of designs based on their associated objective function values $f(x)$ and constraints $g(x)$. In a generic optimisation these objectives and constraints could be evaluated from an analytical equation to link the input variables to the output variables. In this implementation the objectives and constraints are evaluated from a computational fluid dynamics (CFD) simulation of the parametric geometry. This in-the-loop CFD process requires more computational resource than the use of a surrogate model based on integral parameters. However, it also provides a higher fidelity drag estimation and allows for optimisation of the aerodynamic characteristics. The optimisation was carried out with a Gaussian mutation operator with a muta-

tion rate of 0.2 and mutation size of $\sigma = 0.0005$. The crossover was carried out using the $BLX-\alpha$ operator with $\alpha = 0.5$ which results in an even split between the two parent designs [33].

For each design produced within the optimisation process a multi-grid mesh was produced and CFD simulations performed. To enable the calculation of the off design performance, the designs were simulated at a series of different freestream Mach numbers and two MFCRs. This resulted in ten separate solutions computed for each design. Each optimisation process consisted of 1560 different designs, so in total to optimise the fan cowl, for a specified length (l_{nac}/r_{hi}) and radius ratio (r_{TE}/r_{hi}), 15600 CFD computations were performed.

2.3. CFD method and nacelle drag extraction

The CFD model used to assess the different nacelle designs consisted of an axisymmetric 2D nacelle, a bypass and core exhaust nozzle and a semi-circular farfield. The farfield boundary condition was set to represent the freestream flow of the engine in flight. The freestream Mach number is varied in this study, but static pressure and temperatures are fixed to an International Standard Atmosphere day at 35000 feet, with a freestream turbulent intensity of 0.1%. A Reynolds-Averaged Navier-Stokes (RANS) solver, ANSYS Fluent v15.0[34], was used for the assessment of the nacelle aerodynamics. This used a density based implicit method which solved the RANS equations closed with the $k-\omega$ SST turbulence model with a second order discretisation scheme. A Roe-FDS scheme was used with Green-Gauss node based discretisation. A structured multi-grid approach was taken to produce a computational mesh of the geometries. A multi block structured mesh was used to ensure that the mesh quality did not vary too much between designs. The boundary layers of the fan cowl, intake and spinner were fully resolved with a y^+ value below 1. The other wall surfaces, associated with the exhaust system, were modelled as slip walls to reduce mesh

size. The mesh generation and CFD process was fully automated to enable in-the-loop CFD computations for optimisation.

Nacelle drag (C_{Dnac}) was calculated from the RANS solutions with a near-field approach [35]. The definition of drag used for the calculations is in accordance with the thrust drag accounting standard defined by AGARD [36]. With this near field approach the pre-entry force (ϕ_{pre}) and the cowl force (ϕ_{cowl}) (Figure 1) are calculated concurrently which removes the need to find the pre-entry stagnation point. The post-exit force was calculated by direct pressure integration along the dividing streamline from the nacelle trailing edge.

Numerical convergence was achieved through a steady increase of the Courant-Friedrichs-Lewy number throughout the iterative process. This iterative convergence was monitored and solutions considered to be converged once the normalised residuals were below 10^{-5} relative to the initialised case. A mesh independence study was carried out with three meshes (36k, 72k, 144k) based on the nacelle drag (C_{Dnac}). The drag was assessed for the nacelle at the cruise condition ($M_\infty = 0.85$, MFCR = 0.7). In accordance with the recommendation from Roache [37], the error relative to the Richardson extrapolation was calculated to be less than 1% for the medium sized grid (Table 2). This grid was therefore used for all optimisation studies. In addition to this, a domain independence study was carried out with four domain sizes ($40r_{max}$,$60r_{max}$,$80r_{max}$,$100r_{max}$), again focused on the drag (C_{Dnac}) value of the nacelle. It was decided to use a semi-circular domain with a radius of $80r_{max}$ as there was a 0.7% change in the calculated drag between the cases with $80r_{max}$ and $100r_{max}$ (Table 3). A previous study has demonstrated the accuracy of this method relative to experimental data[38]. This work demonstrated the importance of modelling the exhaust system and jet to correctly capture the pressure field of the nacelle. The previous study compared 4 nacelles of varying nacelle lengths ($l_{nac}/r_{hi} = 3.6$

to $l_{nac}/r_{hi} = 6.7$). The validation was also carried out on a mix of axisymmetric and non-axisymmetric geometries and at a range of zero and non-zero incidences. Whilst the present study only considers axisymmetric nacelles at zero incidence, the same meshing standards were read across from the preceding study so the conclusions are expected to be valid. Overall, this study has shown that the CFD method and process used in this study is useful for the analysis of nacelle aerodynamics and validation studies show that the method provides a maximum uncertainty of up to 4% on pre-drag-rise nacelle drag, a difference of ± 0.003 on M_{DR}, at a representative MFCR of 0.7, and typically an over prediction of critical MFCR of up to 2% [38, 39]. The previous study also includes a comparison of outer nacelle surface isentropic Mach number values between the CFD model prediction and experimental test data. These comparisons, performed at incidences representative of cruise, demonstrated a good overall agreement between CFD and experimental test measurements, with a difference in peak Mach numbers within $M = 0.01$.

Configurations	Coarse	Medium	Fine
Cells	35870	71344	144712
C_{Dnac}	0.02783	0.02354	0.02351

Table 2: Results from the CFD simulations of 2-dimensional axisymmetric nacelle meshes produced for independence studies

Domain Size	$40r_{max}$	$60r_{max}$	$80r_{max}$	$100r_{max}$
C_{Dnac}	0.0248	0.0246	0.0242	0.0241

Table 3: 2-dimensional axisymmetric nacelle meshes produced for domain independence study

2.4. Optimisation metrics

The convergence of the optimisation process was measured as a function of the generation to determine if it had suitably converged to near the Pareto opti-

mal set. To measure this level of convergence the hypervolume was monitored. Hypervolume is a metric which is a combined measure of the convergence and the diversity in the solution since it increases with both of these measures [33]. It is calculated as an m-dimensional volume bounded by the Pareto set and a reference value.

2.5. Performance metrics

Three metrics were used to optimise the aerodynamic performance of the nacelles throughout the optimisation. The first of these was the nacelle cruise drag ($C_{Dcruise}$), calculated at $M_\infty = 0.85$, $MFCR = 0.7$ and $h = 10668m$ (equation 5). The second metric was the drag rise Mach number (M_{DR}) (equation 6). The drag rise Mach number determines the freestream Mach number above which wave drag increases rapidly. Nacelles are typically designed to operate below this Mach number and a typical margin of safety used is $\Delta M = 0.02$ [12]. Since the desired cruise Mach number for the optimisation designs is $M_\infty = 0.85$ the target drag rise Mach number is $M_{DR} > 0.87$. The third performance metric, spillage drag (c_{Dspill}) (equation 7), determines the influence of the nacelle drag as the MFCR is decreased. In this case the value is taken as a change in drag between the cruise $MFCR = 0.7$ and $MFCR = 0.63$. For the engine cycle used in this study this change in mass flow results in a throttled down engine of 55% of the cruise thrust. This is somewhere between the end of cruise power setting at constant altitude and the idle condition used for start of descent.

$$c_{Dcruise} = \frac{D_{nac}\Big|_{M_\infty=0.85, MFCR=0.7, h=10668m}}{0.5 q_\infty A_{hi}} \tag{5}$$

$$\frac{\partial C_D}{\partial M_\infty}\bigg|_{M_{DR}} = 0.1 \tag{6}$$

$$c_{Dspill} = \frac{D_{nac}\Big|_{M_\infty=0.85,MFCR=0.63,h=10668m}}{0.5q_\infty A_{hi}} - \frac{D_{nac}\Big|_{M_\infty=0.85,MFCR=0.7,h=10668m}}{0.5q_\infty A_{hi}} \tag{7}$$

2.6. Aerodynamic metrics

In addition to the aerodynamic drag and related metrics (section 2.5) two metrics were calculated which related directly to the pressure distributions on the nacelle. The first metric of interest (equation 8) was the sum of the peak pressure coefficient upstream of the shock across the m number of shocks present on the cowl. This should provide an additional penalty to designs with high wave drag and also exclude designs which have several sonic regions. The second metric of interest (equation 9) quantified the number of points at which the gradient changed polarity in the pressure distribution since a conventional design should ideally only do this once [9]. Specifically, it calculated the total number of gradient ($\delta C_p/\delta x$) polarity changes and summed the magnitude of the second derivative at this polarity change (λ). When a constraint was applied to the former metric (C_{shock}) it limited the shock strength allowed on the nacelle. Minimisation of the latter metric ($C_{inflect}$) results in designs with increasingly monotonic pressure distributions.

$$C_{shock} = \sum_m |c_p| \tag{8}$$

$$C_{inflect} = \sum_n |\lambda| \tag{9}$$

3. Results and analysis

3.1. Optimisation without constrained pressure distributions

An optimisation was carried out for a non-dimensional nacelle length of $l_{nac}/r_{hi} = 3.8$ at a cruise Mach number of $M_\infty = 0.85$ and $MFCR = 0.7$. This represents a relatively conventional and conservative nacelle length and is chosen to first demonstrate the overall optimisation system. A 1979 study on nacelle aerodynamics [8] focussed on nacelles around the length of $l_{nac}/r_{hi} = 6.73$. For comparison, the study by Fang et al [17] considered a length of approximately $l_{nac}/r_{hi} = 3.28$ to operate at $M_\infty = 0.8$. Some example in service nacelles, designed to operate at a cruise Mach number of $M_\infty = 0.82$, have lengths of $l_{nac}/r_{hi} = 3.92$ and $l_{nac}/r_{hi} = 3.38$ respectively [40]. In this context, the length of $l_{nac}/r_{hi} = 3.8$ is a relatively conservative length however it is aimed to operate at a higher Mach number of $M_\infty = 0.85$. The bounds used for this optimisation, summarised in Table 1, were chosen to cover a wide range of the available design space and to expand beyond conventional design parameters. The engine was designed to cruise at a flight $M_\infty = 0.85$, which once a conservatism factor [12] is considered the drag rise Mach number should be above $M_{DR} = 0.87$. A constraint of $M_{DR} > 0.85$ was therefore applied to resolve this difficult region of the design space. The hypervolume of the Pareto set was calculated at each generation to determine the level of convergence of the optimisation process. 30 generations were computed and over the final 5 generations there was less than a 1% increase in hypervolume which indicated that the optimisation was converged close to the optimal set.

The optimisation process ultimately produced a Pareto set of individual designs (Figure 3). This Pareto set spans a range of $c_{Dcruise}$, c_{Dspill} and M_{DR} values which are all equally optimal, which demonstrates that a trade-off exists between the three chosen objective functions and a final design would be

chosen to suit specific requirements. The highest drag rise Mach number was $M_{DR} = 0.885$ which was limited by the range of Mach numbers computed for each case. Since the highest Mach number computed was $M_\infty = 0.89$ the highest Mach number at which the gradient was calculated was $M_\infty = 0.885$. To ensure that the optimisation algorithm has correctly identified good designs and better designs are found throughout the generations, the final Pareto set can be compared to the random initialisation population. The improvement from the initial generation, resulted in an increase in M_{DR} from $M_{DR} = 0.8672$ to $M_{DR} = 0.8716$. The mean value of drag ($c_{Dcruise}$) reduced by $\Delta c_{Dcruise} = 0.0009$ from $c_{Dcruise} = 0.0313$ to $c_{Dcruise} = 0.0304$, however the mean spillage (c_{Dspill}) increased from $c_{Dspill} = 0.0027$ to $c_{Dspill} = 0.0040$ as the optimisation populated the objective space with designs which met the drag rise objective. This indicated that the population increased disproportionately in the higher M_{DR} region or that the initial population was skewed to the lower spillage regions. NSGA-II has been observed to exhibit uneven distributions across a Pareto set in comparison to some similar algorithms [41], however good convergence is still achieved. The minimum spillage drag which met the criterion of $M_{DR} = 0.87$ decreased by $\Delta c_{Dspill} = 0.0011$ from $c_{Dspill} = 0.0016$ to $c_{Dspill} = 0.0005$. The results of this optimisation demonstrate that the higher drag rise Mach numbers are achieved at the expense of the spillage drag performance. The lower values are achieved at the expense of higher mid cruise drag (Figure 3).

For example, if a cruise Mach number of $M_\infty = 0.84$ is required then a drag rise Mach number of $M_{DR} = 0.86$ would be typically considered. The optimisation process has resulted in designs which meet this criterion (Figure 3) and have generally favourable aerodynamics, i.e. no strong shocks or separation at cruise (Figure 4). With the requirement of $M_{DR} \geq 0.86$ there is still a trade-off between the cruise drag and the spillage drag. A lower cruise drag can

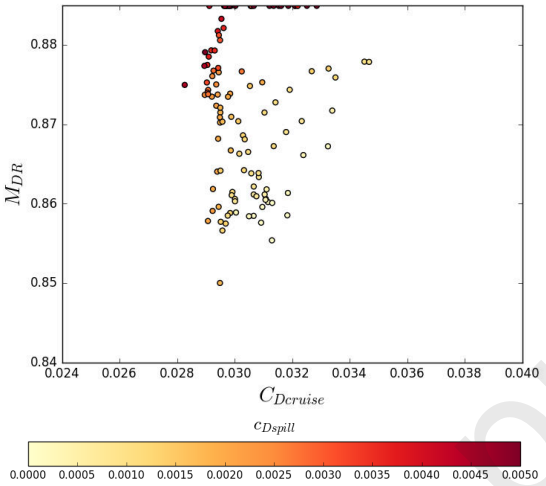

Figure 3: Pareto optimal sets for optimisation performed at nacelle length of $l_{nac}/r_{hi} = 3.8$, and radius ratio of $r_{TE}/r_{hi} = 0.911$ plotted as a function of the performance metrics

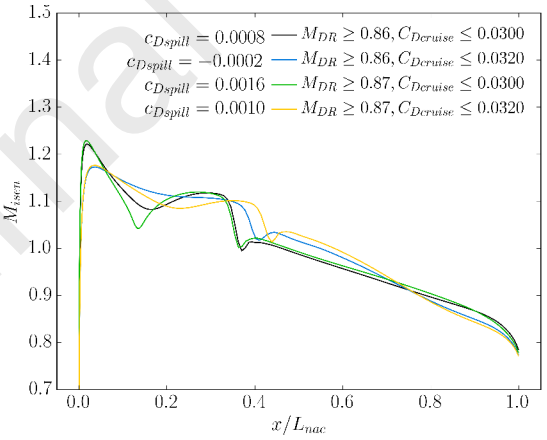

Figure 4: Example optimal fan cowl Isentropic Mach number profiles at a length of $l_{nac}/r_{hi} = 3.8$ and radius ratio of $r_{TE}/r_{hi} = 0.911$ for different required M_{DR} and $C_{Dcruise}$

be achieved at the expense of both the spillage drag (Figure 3) and the Mach number distribution (Figure 4). An increase in the acceptable $C_{Dcruise}$ from $C_{Dcruise} \leq 0.0300$ to $C_{Dcruise} \leq 0.0320$ for example resulted in a reduced peak Mach number from $M_{peak} = 1.22$ to $M_{peak} = 1.17$. This gave a concomitant reduction in spillage drag from $C_{Dspill} = 0.0008$ to $C_{Dspill} = -0.0002$ (Figure 7b). As the required M_{DR} is increased the minimum spillage penalty are also increased (Figure 3). An increase in the desired operational Mach number to $M_{\infty} = 0.85$ and the requisite increase to $M_{DR} = 0.87$ also begins to make the aerodynamics of the possible designs noticeably less favourable (Figure 4). The aerodynamic behaviour becomes characterised by multiple accelerations and wave drag during the cruise operation. As at the lower required M_{DR}, the decision of an acceptable $C_{Dcruise}$ has a strong influence on the spillage and the pressure distributions. For example, an increase in the acceptable $C_{Dcruise}$ from $C_{Dcruise} \leq 0.0300$ to $C_{Dcruise} \leq 0.0320$ resulted in optimal designs with a reduced peak Mach number from $M_{peak} = 1.23$ to $M_{peak} = 1.18$ and a reduction in spillage drag from $C_{Dspill} = 0.0016$ to $C_{Dspill} = 0.0010$ (Figure 7b). Overall, even for this relatively conventional nacelle $l_{nac}/r_{hi} = 3.8$, this example highlights the typical trade-off that is considered during a nacelle design. For example there is a strong trade off between spillage and M_{DR} which results in being much more difficult to design a good nacelle with a high M_{DR}. Similarly, depending on the application, there is a trade-off between $C_{Dcruise}$ and the acceptable C_{Dspill}. The optimisation method has identified these characteristics while also linking the overall metrics to desirable isentropic Mach distributions at the lower required drag rise values.

The second nacelle length assessed using the optimisation method had $l_{nac}/r_{hi} = 3.1$ which is in a more aggressive region of the design space than the previous length $l_{nac}/r_{hi} = 3.8$ and those reported in the open source. The same

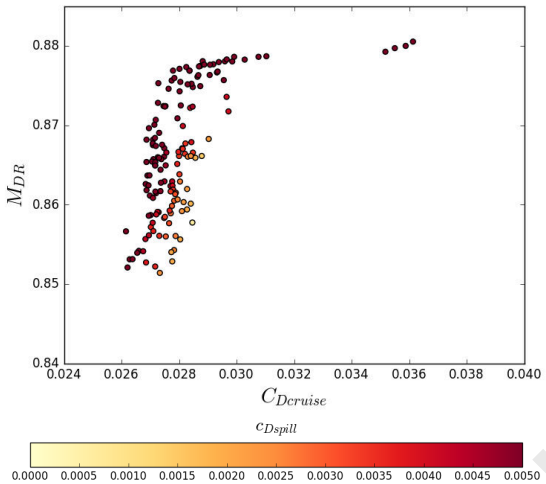

Figure 5: Pareto optimal sets for optimisation performed at nacelle length of $l_{nac}/r_{hi} = 3.1$ and radius ratio of $r_{TE}/r_{hi} = 0.911$, plotted as a function of the performance metrics

bounds were used for all five variables [β, r_{max}, l_{fb}, r_{if}, y''_{TE}] as were used for the optimisation of the longer nacelle ($l_{nac}/r_{hi} = 3.8$) (Table 1). Again the convergence of the optimisation procedure was monitored by the hypervolume across all 30 generations. Over the final 5 generations there was less than a 0.1% increase in the hypervolume, which again indicated a good level of convergence from the algorithm. The evolution from the initial random sample resulted in a $\Delta M_{DR} = 0.004$ higher mean value of M_{DR} with an increase from $M_{DR} = 0.867$ to $M_{DR} = 0.881$. The mean value of cruise drag ($C_{Dcruise}$) reduced by $\Delta c_{Dcruise} = 0.0028$ from $c_{Dcruise} = 0.0311$ to $c_{Dcruise} = 0.0283$, whilst the mean spillage (c_{Dspill}) decreased by $\Delta c_{Dspill} = 0.0048$ from $c_{Dspill} = 0.0101$ to $c_{Dspill} = 0.0053$. No individuals in the initial random design space exceeded a drag rise Mach number of $M_{DR} = 0.87$. However after the optimisation 34% of the Pareto set had the desired drag rise Mach number of $M_{DR} \geqslant 0.87$ with the minimum spillage of $c_{Dspill} = 0.0040$ for a design which meets the drag rise criterion of $M_{DR} \geqslant 0.87$ (Figure 7a). It is clear from the Pareto set (Figure 5) that the optimal designs at this shorter nacelle length ($l_{nac}/r_{hi} = 3.1$) allow for

around 10% lower nacelle drag compared with the longer length ($l_{nac}/r_{hi} = 3.8$). This is to be expected since there is less wetted area for a shorter nacelle and the skin friction drag of the nacelle typically accounts for 50-60% of the nacelle drag. However, these optimal designs also demonstrate that reaching the higher values of drag rise Mach numbers is more penalising to the spillage drag further emphasising the need for multi-objective optimisation. This also resulted in less desirable pressure distributions on the nacelle surface which produced this additional wave drag at higher freestream Mach numbers and the lower $MFCR = 0.65$. This highlights the increased difficulty in designing a nacelle of shorter length as the spillage drag (c_{Dspill}) is around twice as large at $M_{DR} = 0.87$ for the shorter length ($l_{nac}/r_{hi} = 3.1$) in comparison to the longer nacelle ($l_{nac}/r_{hi} = 3.8$).

3.2. Optimisation with directly optimised pressure distributions

The optimisations for the two nacelle lengths were repeated with the limitations on the aerodynamic pressure distributions which were outlined in section 2.6. This provided an additional constraint, limiting the factor $C_{shock} < 0.8$ which prevented the sum of pre-shock c_p from exceeding -0.8, and an additional objective function to minimise $C_{inflect}$. These two additional controls were expected to limit the designs within the final Pareto set to configurations with weaker shocks and smoother pressure distributions compared to the optimisations without these constraints (section 3.1). Due to the added objective ($C_{inflect}$) and the additional constraint (C_{shock}), the generation size was increased from 40 to 50. The geometric bounds of the optimisation were kept the same (Table 1).

The addition of the controls (C_{shock}, $C_{inflect}$) resulted in higher values of M_{DR} found for the short nacelle ($l_{nac}/r_{hi} = 3.1$)(Figure 6a) relative to the unconstrained optimisation shown previously (Figure 5). Whereas the uncon-

strained optimisation had a maximum M_{DR} of $M_{DR} = 0.880$ the constrained optimisation resulted in designs which had the maximum M_{DR} of $M_{DR} = 0.885$. However, above $M_{DR} = 0.87$, the minimum cruise drag is around 4% higher than the optimisation without the two additional metrics (C_{shock}, $C_{inflect}$). This indicates that the lowest cruise drag ($c_{Dcruise}$) designs have undesirable aerodynamic distributions which are mitigated in the more constrained optimisation hence they have been removed from the constrained Pareto set. There is also an increase in the average drag for the longer nacelle once the constraints are applied (Figure 6b) relative to the unconstrained optimisation (Figure 3).

To understand the changes incurred by the addition of the pressure limitations (C_{shock}, $C_{inflect}$) comparable designs were chosen from the unconstrained Pareto sets and the constrained sets for the short nacelle length of $l_{nac}/r_{hi} = 3.1$. These were chosen to meet a range of requirements, specifically two target drag rise Mach numbers ($M_{DR} \geq 0.86$ and $M_{DR} \geq 0.87$) and two target cruise drag values ($C_{Dcruise} \leq 0.0300$ and $C_{Dcruise} \leq 0.0320$). The nacelle design with the lowest spillage drag which also met these requirements was selected from the two Pareto sets. The controls on the pressure distributions (C_{shock}, $C_{inflect}$) produced, in general, designs with isentropic Mach number distributions that had less severe pressure gradients (Figure 8). The introduction of the pressure distribution controls reduced the peak Mach numbers on all four nacelle designs significantly (Figures 8a, 8b). As a result the sum of the pre-shock Mach numbers on the constrained designs was reduced relative to the unconstrained designs.

At the lower required M_{DR} of $M_{DR} \geq 0.86$ there was either equivalent or better spillage performance between the optimisations with and without the aerodynamic constraints outlined in section 2.6. At a required $M_{DR} \geq 0.86$ and $C_{Dcruise} \leq 0.0280$ the spillage decreased from $c_{Dspill} = 0.0025$ to $c_{Dspill} =$

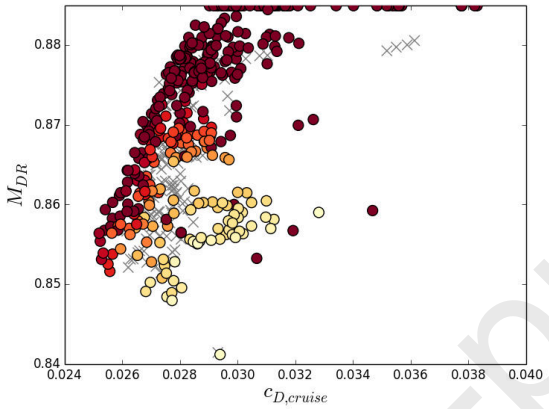

(a) $l_{nac}/r_{hi} = 3.1$, $r_{TE}/r_{hi} = 0.911$

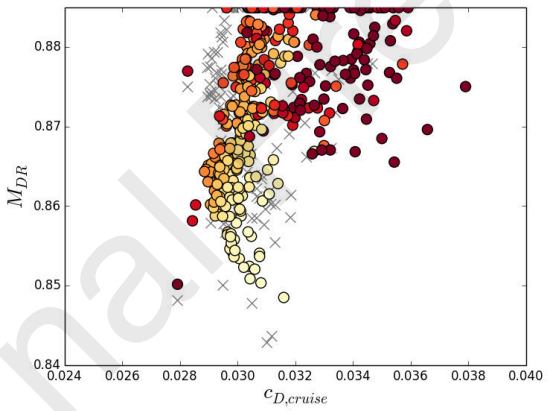

(b) $l_{nac}/r_{hi} = 3.8$, $r_{TE}/r_{hi} = 0.911$

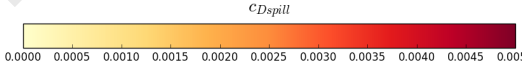

Figure 6: Pareto optimal sets for optimisations performed at two different lengths with pressure limitations (C_{shock}, $C_{inflect}$), plotted as a function of the performance metrics (o), with the Pareto sets from the optimisations without pressure limitations shown in grey (x)

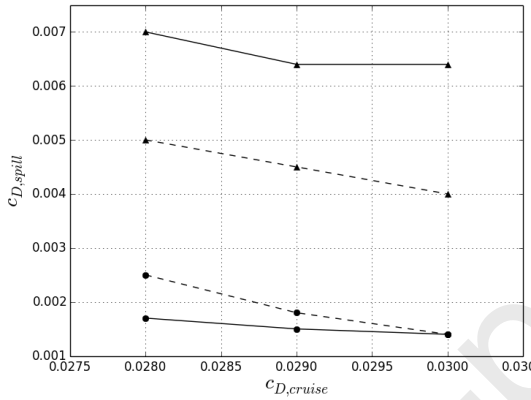

(a) $l_{nac}/r_{hi} = 3.1$, $r_{TE}/r_{hi} = 0.911$

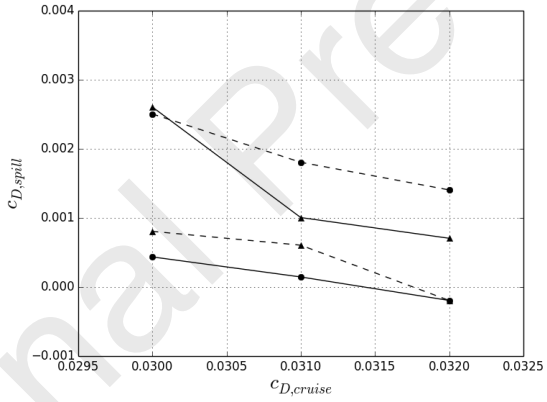

(b) $l_{nac}/r_{hi} = 3.8$, $r_{TE}/r_{hi} = 0.911$

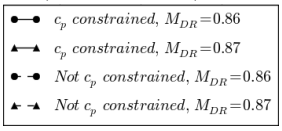

Figure 7: Minimum achievable c_{Dspill} for different nacelle lengths and different required levels of $c_{Dcruise}$ and M_{DR}

0.0017 through the addition of aerodynamic constraints (Figure 7a). At a required $M_{DR} \geq 0.86$ and $C_{Dcruise} \leq 0.0300$ the spillage remained unchanged at $c_{Dspill} = 0.0014$. However at the higher required M_{DR} of $M_{DR} \geq 0.87$, whilst the aerodynamics had more conventional distributions the spillage was worsened through addition of the aerodynamic constraints. Specifically, at a required $M_{DR} \geq 0.87$ and $C_{Dcruise} \leq 0.0280$ the spillage increased from $c_{Dspill} = 0.0050$ to $c_{Dspill} = 0.0070$ through the addition of aerodynamic constraints and at $C_{Dcruise} \leq 0.0300$ it increased from $c_{Dspill} = 0.0040$ to $c_{Dspill} = 0.0064$ (Figure 7a). This is due to the unconstrained optimal designs exhibiting relatively unstable pressure distributions which when subjected to lower MFCRs changed the shock topology from a double shock pattern to a single shock pattern. This response, whilst providing improved spillage, is not desirable as it likely to result in sudden changes in drag across the operating envelope. This is evidenced in the nacelle drag as a function of freestream Mach number (Figure 9). The designs which came from the unconstrained optimisations were far more sensitive to changes in the freestream Mach number whereas the designs from the constrained optimisations had a monotonic relation between C_{Dnac} and M_{∞}. A danger of optimisation, even multi-objective optimisation, is that the resultant designs will be over-designed for the metrics which are given as objectives. The introduction of the aerodynamic constraints evidently reduces this somewhat by penalising pressure distributions which aren't smooth. In comparison with the more conventional configurations, the viable design space is relatively restricted for a short nacelle ($l_{nac}/r_{hi} = 3.1$) with an aggressive trailing edge radius ratio of $r_{TE}/r_{hi} = 0.911$. Although the addition of additional aerodynamic constraints based on the expected desirable Mach number distributions improve some of the metrics, it is still a difficult part of the design space.

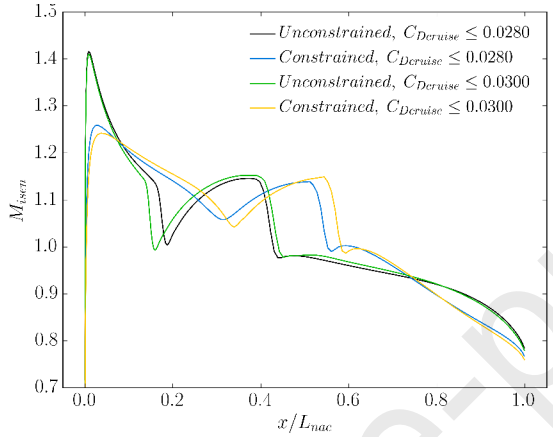

(a)

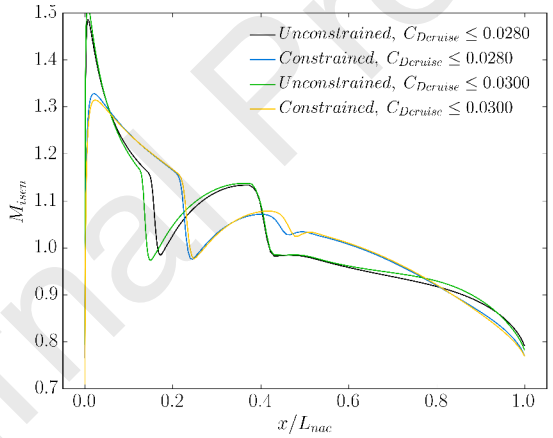

(b)

Figure 8: Example optimal Isentropic Mach number profiles at a length of $l_{nac}/r_{hi} = 3.1$ and radius ratio of $r_{TE}/r_{hi} = 0.911$ with (a) a required $M_{DR} \geqslant 0.86$ and (b) a required $M_{DR} \geqslant 0.87$

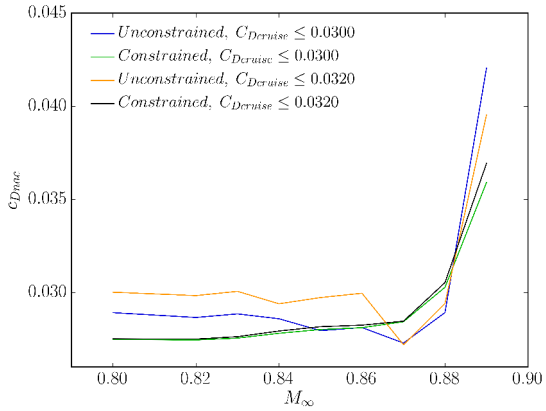

Figure 9: C_{Dnac} as a function of M_∞ for designs with different $C_{Dcruise}$ criteria for a nacelle length of $l_{nac}/r_{hi} = 3.1$ and radius ratio of $r_{TE}/r_{hi} = 0.911$ with and without aerodynamic constraints at a required $M_{DR} \geqslant 0.87$

3.3. Influence of length and trailing edge offset on optimal designs

The previous analyses highlighted some of the MOO challenges that arise for a nacelle design. In particular, the significant increase in the design difficulty when the M_{DR} is increased which is exacerbated when the nacelle length (l_{nac}/r_{hi}) is reduced. In these more difficult parts of the design space, it is also useful to consider the characteristics of the nacelle surface lift distributions. Although the implementation of additional design constraints on the lift distributions can improve the aerodynamic characteristics, there are still some undesirable features which highlight the difficulty of the design for this nacelle length and flight Mach number. Consequently, it is of interest to understand how the design space is affected by a change in the geometry bounds and if the optimisation method can identify designs with desirable aerodynamics characteristics. Since the optimisation starts from a prescribed trailing edge and highlight position the length and radial offset ($r_{TE} - r_{hi}$) are prescribed. To determine the influence of the trailing edge radius on the aerodynamic performance of a nacelle a series of three trailing edge radii ($r_{TE}/r_{hi} = 0.911$,$r_{TE}/r_{hi} = 0.95$,$r_{TE}/r_{hi} = 1.0$) were optimised for both lengths ($l_{nac}/r_{hi} = 3.1$ and $l_{nac}/r_{hi} = 3.8$). An in-

crease in the trailing edge radius reduces the radial offset which must be achieved by the optimal fan cowl curve. It would be expected that this should reduce the overall amount curvature and therefore provide a design with lower surface isentropic Mach numbers.

Each of these optimisations incorporated the c_p controls (C_{shock}, $C_{inflect}$) described in section 2.6. The outcome of these six optimisations were six Pareto sets (Figure 6b, 10) which enabled a comparison of the optimal designs available for each length and trailing edge radius. As before, the designs with the highest drag rise Mach number were also those with the most adverse spillage as the requirement to minimise the frontal facing area of the nacelle to improve the M_{DR} also makes the accelerations around the lip more severe and the spillage worse. However for both lengths ($l_{nac}/r_{hi} = 3.1$ and $l_{nac}/r_{hi} = 3.8$) the spillage at higher M_{DR} is reduced by an increase in the trailing edge radius.

To compare these data it is useful to consider the possible designs available given a particular design requirement, in this case M_{DR} (Figure 11). The drag and spillage of the shorter ($l_{nac}/r_{hi} = 3.1$) nacelle rapidly worsens as a higher M_{DR} is targeted (Figure 11). For instance, at a required $M_{DR} = 0.855$ the achievable level of drag for the shortest nacelle ($l_{nac}/r_{hi} = 3.1$), with a low trailing edge radius ($r_{TE}/r_{hi} = 0.911$), is $c_{Dcruise} = 0.0252$ (Figure 11a). Conversely, the longer nacelle ($l_{nac}/r_{hi} = 3.8$) with the same trailing edge radius ($r_{TE}/r_{hi} = 0.911$) had a minimum achievable drag of $c_{Dcruise} = 0.0289$. This is an improvement from a shorter nacelle of $\Delta c_{Dcruise} = -0.0037$. However, if the required drag rise was increased to $M_{DR} = 0.88$ then the improvement in drag available from a shorter nacelle would decrease by 70% to $\Delta c_{Dcruise} = -0.0011$ which reflects the increased difficulty in producing a good design for a short nacelle at high Mach numbers. A similar problem is evident in the spillage drag at different drag rise Mach numbers (Figure 11b). For a required $M_{DR} = 0.855$

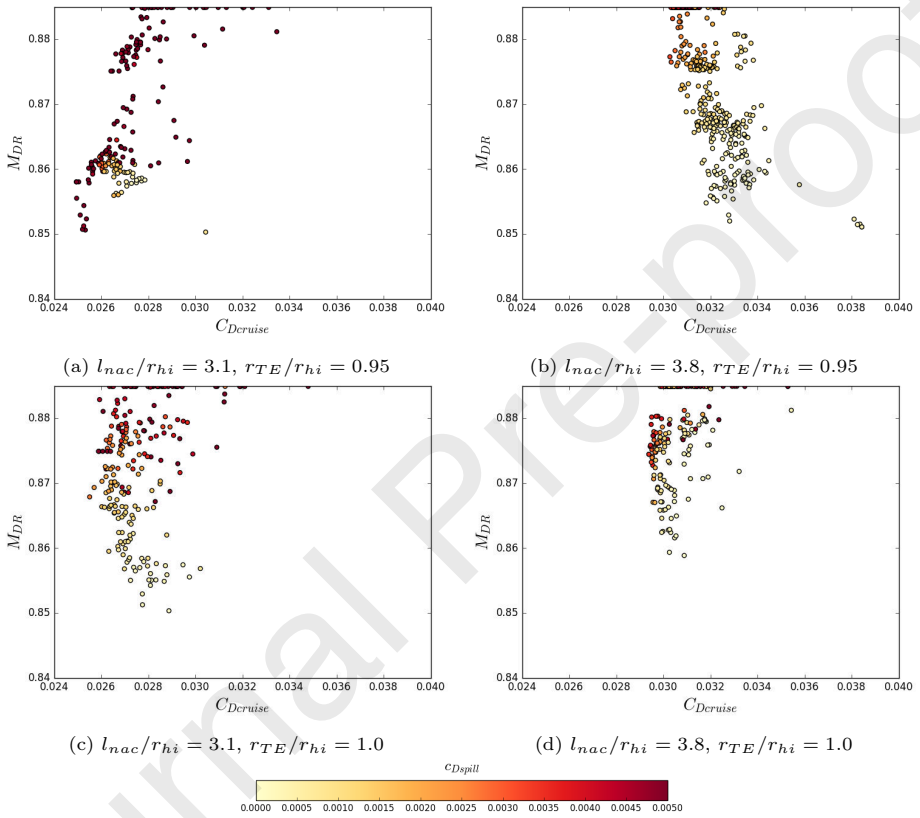

(a) $l_{nac}/r_{hi} = 3.1$, $r_{TE}/r_{hi} = 0.95$

(b) $l_{nac}/r_{hi} = 3.8$, $r_{TE}/r_{hi} = 0.95$

(c) $l_{nac}/r_{hi} = 3.1$, $r_{TE}/r_{hi} = 1.0$

(d) $l_{nac}/r_{hi} = 3.8$, $r_{TE}/r_{hi} = 1.0$

Figure 10: Pareto optimal sets for optimisations performed at different lengths and trailing edge radii, plotted as a function of the performance metrics

the minimum spillage which can be attained for both nacelle lengths is below $c_{Dspill} = 0.0001$. However, the performance of the short nacelles is far worse at the higher drag rise Mach numbers and by $M_{DR} = 0.88$ the minimum spillage from the short nacelle is $c_{Dspill} = 0.0070$ which would represent around a quarter of the cruise drag. The longer nacelle on the other hand has a less detrimental response to an increase in the required M_{DR}. As a result, the minimum spillage at $M_{DR} = 0.88$ is $c_{Dspill} = 0.0016$ which indicates the relative ease of design. The influence of the trailing edge radius is also evident, most notably for the short nacelle. For the optimisations on the short nacelle the lowest trailing edge radius ($r_{TE}/r_{hi} = 0.911$) resulted in the highest drag and spillage at $M_{DR} = 0.88$. This is a substantial rise from the minimum value at $M_{DR} = 0.855$. With an increase in the trailing edge radius to $r_{TE}/r_{hi} = 1.0$ the gradient of minimum cruise drag as a function of M_{DR} decreases which results in a much improved drag at $M_{DR} = 0.88$ relative to the lower trailing edge $r_{TE}/r_{hi} = 0.911$. Specifically, this increase in trailing edge radius from $r_{TE}/r_{hi} = 0.911$ to $r_{TE}/r_{hi} = 1.0$ allows a minimum drag of $c_{Dcruise} = 0.0259$ at $M_{DR} = 0.880$ compared to $c_{Dcruise} = 0.0285$ for the lower trailing edge radius.

The reason for the different performances across the range of lengths and trailing edge radii can be explained through the aerodynamic loadings on the cowl (Figure 12). Six designs were chosen from the Pareto sets which all met the criterion of $M_{DR} > 0.87$. The shortest nacelle ($l_{nac}/r_{hi} = 3.1$) with the lowest trailing edge ($r_{TE}/r_{hi} = 0.911$) had the highest peak Mach number of $M_{peak} = 1.33$. This high peak Mach number results in a stronger shock and additional wave drag. As the MFCR is decreased from MFCR=0.7 and MFCR=0.65 this peak Mach number increases from $M = 1.33$ to $M = 1.46$ and this results in the high spillage value of $c_{Dspill} = 0.0069$. An increase

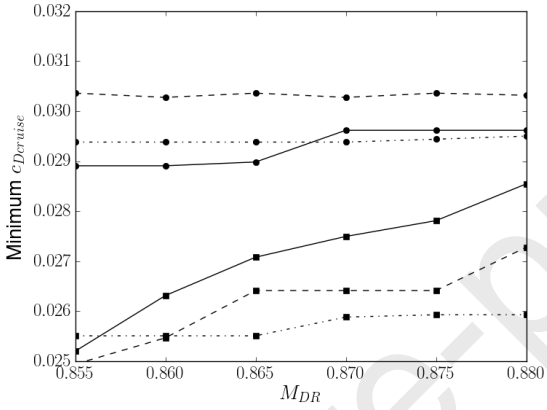

(a)

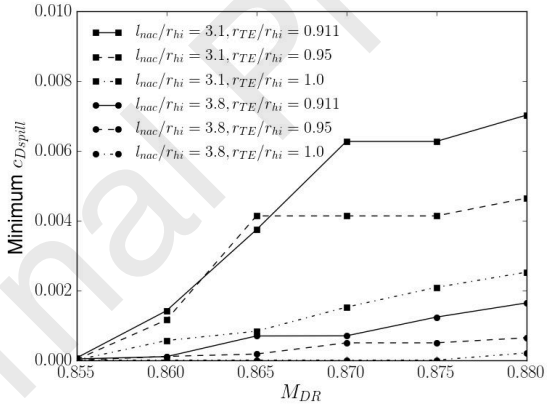

(b)

Figure 11: Minimum achievable (a) $c_{Dcruise}$ and (b) c_{Dspill} for a given M_{DR}

in the length from $l_{nac}/r_{hi} = 3.1$ to $l_{nac}/r_{hi} = 3.8$ improves the isentropic Mach distribution which can be achieved (Figure 12b). A change in the length from $l_{nac}/r_{hi} = 3.1$ to $l_{nac}/r_{hi} = 3.8$ reduced the peak Mach number of the optimal design by $\Delta M = 0.09$ from $M = 1.33$ to $M = 1.24$. This resulted in less wave drag during cruise and less spillage, $c_{Dspill} = 0.0015$ compared to $c_{Dspill} = 0.0069$.

If a designer could not lengthen the nacelle, an alternative would be to increase the trailing edge radius which also improves the peak Mach number. For example, the shortest nacelle length investigated ($l_{nac}/r_{hi} = 3.1$), the improvement in the Mach number distribution from an increase in the trailing edge radius is evident (Figure 12a). In addition to the removal of the double shock pattern by increasing from $r_{TE}/r_{hi} = 0.911$ to $r_{TE}/r_{hi} = 1.0$, the peak Mach number was reduced by $\Delta M = 0.12$ from $M = 1.33$ to $M = 1.21$. In addition, the nacelle design with $r_{TE}/r_{hi} = 1.0$ had $\Delta c_{Dspill} = -0.0053$ (-76%) less spillage and $\Delta c_{Dcruise} = -0.0016$ (-6%) less cruise drag, compared to the nacelle design with $r_{TE}/r_{hi} = 0.911$, whilst still meeting the drag rise criterion of $M_{DR} > 0.87$. A similar influence of trailing edge radius was observed for the longer nacelle (Figure 12b) where the peak Mach number was reduced from $M = 1.24$ to 1.13 by an increase in trailing edge radius from $r_{TE}/r_{hi} = 0.911$ to $r_{TE}/r_{hi} = 1.0$.

The trends in the design space to generate optimal nacelles for different lengths and trailing edge radii were assessed for each of the optimal sets in terms of each degree of freedom (Figure 13). Several key aspects can be determined from these trends which demonstrate the differences in the design approach which could be taken for UHBPR engine nacelles. The longer nacelle designs consistently have larger r_{max}/r_{hi} in the optimal sets, with higher median values for all three trailing edge radii (Figure 13a). In addition an increase in the

trailing edge radius resulted in an increase of the mean value for r_{max}/r_{hi} for the short nacelle, which indicates that as the trailing edge radius is decreased the fineness is reduced to avoid thick and short nacelle designs. Such a trend is less evident for the longer nacelle. In addition to a higher r_{max}/r_{hi}, there was a trend for a greater forebody length ratio (f_{max}) as the trailing edge radius was increased (Figure 13c). The combination of these two parameters determine the start and end points of the forebody. With an increase in the thickness it becomes necessary to have a proportionately longer forebody to avoid high curvatures. The different average values for the design metrics result in different iCST shapes produced. These iCST curves each have a curvature distribution which has been through the solution of the linear set of equations which define the iCST curve (section 2.1). The curvature (κ) distributions which define the fan cowl geometry have a first order influence on the aerodynamics since they determine the amount of local diffusion and compression around the nacelle. The curvature distributions of the optimal nacelles which were chosen from the Pareto fronts all exhibit some similar features (Figure 14). For instance the forebody curvatures of all six designs are monotonic (Figure 14a). The peak acceleration will always occur around the lip and all six of the chosen designs exhibit a peak Mach number just after this. The monotonic curvature distribution which follows this allows a smooth deceleration. This is important in cruise and also in an off design conditions where it is also important to avoid a shock too close to the position of maximum Mach number. To achieve a similar profile of curvature for three different trailing edge radii, whilst avoiding an inflecting afterbody curve, the maximum radius is increased and moved axially rearwards. Five of the six Pareto sets have an average initial forebody radius (f_{if}) of around 0.85 except for the optimal set for the shortest nacelle with the lowest trailing edge radius where on average $f_{if} = 0.95$. Non-dimensionally

this makes a blunter nacelle, however since the radius of curvature (f_{if}) is non-dimensionalised by $l_{fb}/(r_{max} - r_{hi})^2$ and this value is generally higher for the shorter nacelles the dimensional radius of curvature (r_{if}) is similar to the five less aggressive designs.

The highest peaks in isentropic Mach number (Figure 12) correlate with the highest rates of change in curvature (Figure 14b). Subsequent to the peak in $\Delta\kappa/\Delta x$ there is a steady decrease which for all six chosen designs reduced the curvature to less than $\kappa = 0.1m^{-1}$ (Figure 14a). The aft 80% of the nacelle is characterised by small changes in the curvature which mostly remain below $\kappa = 0.1m^{-1}$. In addition, the magnitude of the rate of change of curvature remains below $0.1m^{-2}$ for most of the afterbody until around the last 10% of the cowl.

The boattail angle (β) tended to increase with a greater trailing edge radius for the shorter nacelle whilst the opposite trend was observed for the longer nacelle (Figure 13d). There were no clear trends in the trailing edge second derivative (y''_{TE}) as a function of the length or trailing edge radius. This suggests that either these geometric parameters do not have a first order influence on the performance of the nacelle or that the noise inherent in optimisation has obscured any correlation. Whilst at the cruise condition the afterbody diffusion may not have as much influence on the drag as the forebody design it may be critical at high incidence to prevent separation. Further optimisation work should therefore consider these conditions as well.

4. Conclusions

In this work, a method for nacelle optimisation has been demonstrated which has allowed an understanding of the novel nacelle design space of short fan cowls. The method is based on CFD simulations and thus high fidelity drag

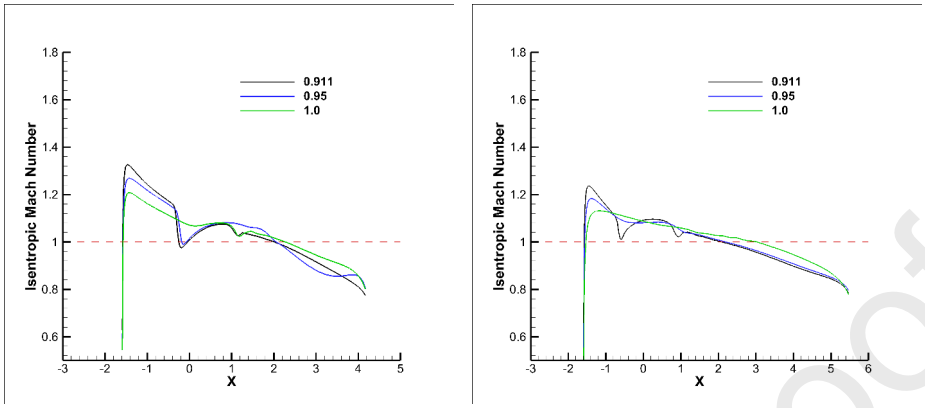

(a) (b)

Figure 12: Example optimal Isentropic Mach number profiles for all trailing edge radii at a length of (a) $l_{nac}/r_{hi} = 3.1$ and (b) $l_{nac}/r_{hi} = 3.8$

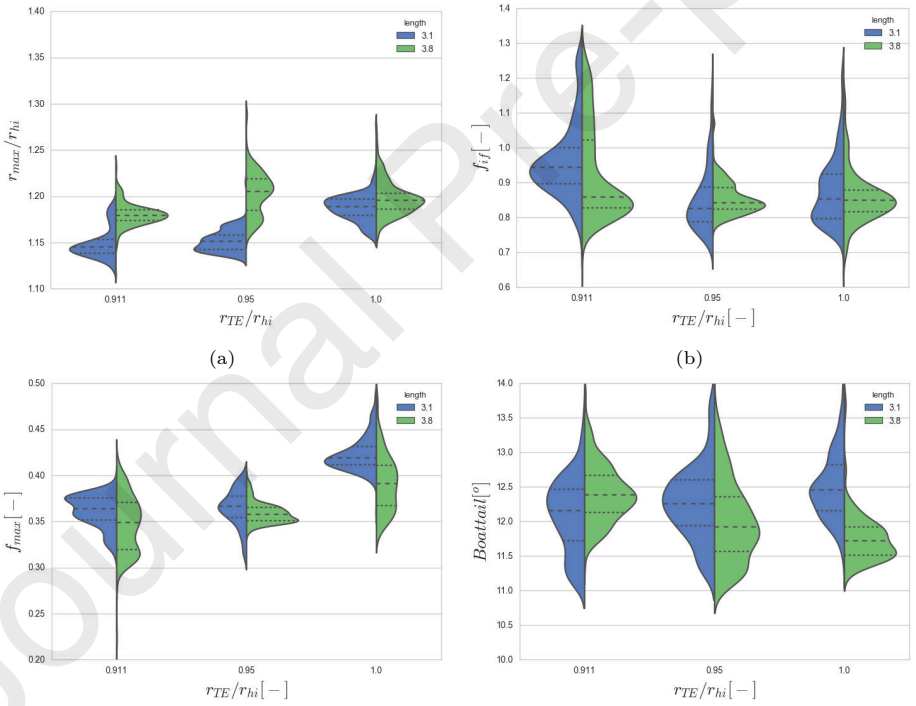

(a) (b)

(c) (d)

Figure 13: Pareto optimal sets for optimisations performed at different lengths and trailing edge radii, plotted as a function of the design metrics. Dashed lines indicate median value and dotted lines indicate the quartiles. Number of individuals are indicated by the relative thickness of the distributions

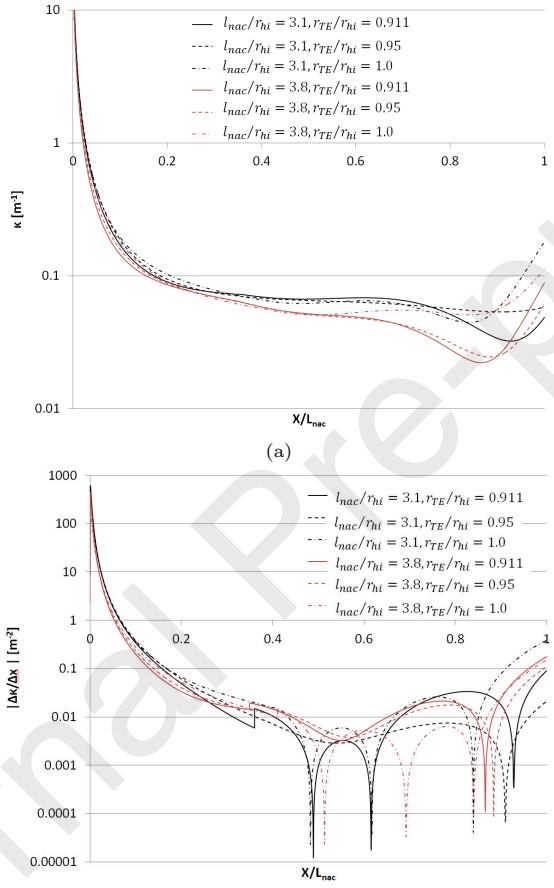

(a)

(b)

Figure 14: (a) Curvature distribution and (b) Rate of change of curvature distribution for six chosen optimal designs for different lengths and trailing edge radii

and Isentropic Mach number distributions are available for each design. The CFD simulations are used to evaluate the fitness of a design directly and with this in-the-loop approach the drag solution is of a high fidelity compared to a surrogate model approach. In addition both performance metrics and pressure distributions are available to be optimised. An improvement to the general method has been proposed which limits the pressure distributions of the fan cowls to more conventional velocity profiles. In effect this is mimicking the work of an inverse design approach but with the capability to reach an optimum without user interaction. Several conclusions can be derived from this optimisation work which are directly pertinent to the design of nacelles for future UHBPR engines. Firstly, a lower trailing edge radius results in optimal design with lower maximum radii. However, given a requirement to achieve a drag rise of $M_{DR} = 0.87$, the most aggressive length nacelles with a high radial offset have unacceptably high peak Mach numbers. This results in very poor off design performance. The nacelle performance can be improved by lengthening or increase of TE radius. Trends in the design space have been assessed for the optimal designs, and one defining feature of the optimal designs is that they all had a monotonic curvature profile for the forebody of the nacelle which results in smooth isentropic Mach number distributions.

5. Acknowledgements

The first author of this paper was partially funded by the Engineering and Physical Sciences Research Council of the United Kingdom. The authors would also like to thank the industrial partner, Rolls-Royce plc for their involvement. Due to commercial confidentiality agreements the supporting data is not available.

References

[1] M. Daly (Ed.), Jane's Aero-Engines, 28th Edition, IHS Global, 2009, p. 64.

[2] J. Marx, Installation features of advanced, very high bypass turbofan propulsion systems, in: AIAA/AHS/ASME/ASEE Aircraft Design, Systems and Operations Conference, no. 89-2141, 1989.

[3] D. Howe, T. Wynosky, Energy efficient engine program advanced turbofan nacelle definition study, Technical Report NASA CR-1/4942, NASA (1985).

[4] F. Majic, G. Efraimsson, C. O'Reilly, Potential improvement of aerodynamic performance by morphing the nacelle inlet, Aerospace Science and Technology 54 (2016) 122–131.

[5] F. Haselbach, A. Newby, R. Parker, Concepts and technologies for the next generation of large civil aircraft engines, in: 29th Congress of the International Council of the Aeronautical Sciences, no. 2014-0078, 2014.

[6] H. Riedel, K. Horstmann, A. Ronzheimer, M. Sitzmann, Aerodynamic design of a natural laminar flow nacelle and the design validation by flight testing, Aerospace Science and Technology 2 (1) (1998) 1–12.

[7] J. Sokhey, Analysis of installed wind tunnel test results on large bypass ratio engine/nacelle installations, in: AIAA/AHS/ASME/ASEE 26th Joint Propulsion Conference, no. 90-2146, 1990.

[8] M. Langley, The design of axisymmetric cowls for podded nacelles for high by-pass ratio turbofan engines, Tech. Rep. Reports and memoranda No. 3846, Aircraft Research Association Ltd, Bedford (1979).

[9] G. Faust, P. Mungur, Nacelle design, in: NASA report for General Electric Company, no. N90-12551/9, NASA, 1987.

[10] A. Petrusson, Aerodynamic evaluation of nacelles for engines with ultra high bypass ratio, Master's thesis, Chalmers University of Technology (2017).

[11] ESDU, Estimation of spillage drag for a wide range of axisymmetric intakes at m<1, Tech. Rep. ESDU 84004, ESDU (1984).

[12] J. Borradaile, Towards the optimum ducted UHBR engine, in: 24th Joint Propulsion Conference, no. 18-2954, 1988.

[13] R. Wilhelm, An inverse design method for engine nacelles and wings, Aerospace Science and Technology 9 (1) (2004) 19–29.

[14] X. Chen, R. K. Agarwal, Shape optimization of airfoils in transonic flow using a multi-objective genetic algorithm, in: 31st AIAA Applied Aerodynamics Conference, no. AIAA 2013-2907, 2013.

[15] W. Wang, R. Mo, Y. Zhang, Multi-objective aerodynamic optimization design method of compressor rotor based on isight, Procedia Engineering 15 (2011) 3699–3703.

[16] H. Toubin, I. Salah El Din, M. Meheut, Multipoint aerodynamic high fidelity shape optimization of an isolated engine nacelle, in: AIAA SciTech 52nd Aerospace Sciences Meeting, no. AIAA 2014-0903, 2014.

[17] X. Fang, Y. Zhang, H. Chen, Transonic nacelle aerodynamic optimization based on hybrid genetic algorithm, in: 17th AIAA/ISSMO Multidisciplinary Analysis and Optimization Conference, no. AIAA 2016-3833, 2016.

[18] W. Song, A. J. Keane, Surrogate-based aerodynamic shape optimization of a civil aircraft engine nacelle, AIAA Journal 45 (10) (2007) 2565–2574.

[19] M. Albert, D. Bestle, Aerodynamic design optimization of nacelle and intake, in: Proceedings of ASME Turbo Expo 2013: Turbine Technical Conference and Exposition, no. GT2013-94857, American Society of Mechanical Engineers, 2013.

[20] J. Wang, J. Cai, Y. Duan, Y. Tian, Design of shape morphing hypersonic inward-turning inlet using multistage optimization, Aerospace Science and Technology 66 (2017) 44–58.

[21] B. M. Kulfan, J. E. Bussoletti, Fundamental parametric geometry representations for aircraft component shapes, in: 11th AIAA/ISSMO multidisciplinary analysis and optimization, AIAA-2006-6948, Renaissance Portsmouth, VA, 2006.

[22] B. M. Kulfan, Universal parametric geometry representation method, Journal of Aircraft 45 (1) (2008) 142–158.

[23] I. Goulos, T. Stankowski, D. MacManus, P. Woodrow, C. Sheaf, Civil turbofan engine exhaust aerodynamics: Impact of bypass nozzle after-body design, Aerospace Science and Technology 73 (2018) 85–95.

[24] T. Zhang, Z. Wang, W. Huang, L. Yan, Parameterization and optimization of hypersonic-gliding vehicle configurations during conceptual design, Aerospace Science and Technology 58 (2016) 225–234.

[25] H. Sobieczky, Parametric airfoils and wings, in: Recent Development of Aerodynamic Design Methodologies, Springer, 1999, pp. 71–87.

[26] F. Zhu, N. Qin, Intuitive class/shape function parameterization for airfoils, AIAA Journal 52 (1) (2013) 17–25.

[27] R. Christie, A. Heidebrecht, D. MacManus, An automated approach to nacelle parameterization using intuitive class shape transformation curves, Journal of Engineering for Gas Turbines and Power 139 (6) (2017).

[28] A. Heidebrecht, T. Stankowski, D. MacManus, Parametric geometry and CFD process for turbofan nacelles, in: Proceedings of ASME 2016 Turbo Expo: Turbomachinary Technical Conference and Exposition, no. GT2016-57784, 2016.

[29] B. Kulfan, A universal parametric geometry representation method - "cst", in: 45th AIAA Aerospace Sciences Meeting and Exhibit, no. AIAA 2007-62, American Institute of Aeronautics and Astronautics, 2007.

[30] I. Goulos, T. Stańkowski, J. Otter, D. MacManus, N. Grech, C. Sheaf, Aerodynamic design of separate-jet exhausts for future civil aero-engines - part i: Parametric geometry definition and computational fluid dynamics approach, Journal of Engineering for Gas Turbines and Power 138 (2016) 1–14.

[31] W. L. MacMillan, Development of a modular type computer program for the calculation of gas turbine off design performance, Ph.D. thesis, School of Mechanical Engineering, Cranfield University (1974).

[32] K. Deb, A. Pratap, S. Agarwal, T. Meyarivan, A fast and elitist multiobjective genetic algorithm: NSGA-II, IEEE Transactions on Evolutionary Computation 6 (6) (2002) 182–197.

[33] K. Deb, Multi-Objective Optimization Using Evolutionary Algorithms, Wiley, 2003.

[34] ANSYS Inc., Ansys fluent theory guide, release 15.0 (November 2013).

[35] R. Christie, S. Ramirez, D. G. MacManus, Aero-engine installation modelling and the impact on overall flight performance, in: Advanced Aero Concepts, Design and Operations, 2014.

[36] MIDAP Study group, Agardograph no. 237 guide to in-flight thrust measurement of turbojets and fan engines, Tech. Rep. AGARD-AG-237, AGARD, by Ministry-Industry Drag Analysis Panel Study Group and others (1979).

[37] P. Roache, Perspective: a method for uniform reporting of grid refinement studies, Journal of Fluids Engineering 116 (3) (1994) 405–413.

[38] M. Robinson, D. MacManus, C. Sheaf, Aspects of aero-engine nacelle drag, Proceedings of the Institution of Mechanical Engineers, Part G: Journal of Aerospace EngineeringPublished online (2018).

[39] T. P. Stańkowski, D. G. MacManus, C. T. Sheaf, R. Christie, Aerodynamics of aero-engine installation, Proceedings of the Institution of Mechanical Engineers, Part G: Journal of Aerospace Engineering 230 (14) (2016) 2673–2692.

[40] Airbus S.A.S., Customer Services, Technical Data Support and Services, 31707 Blagnac Cedex, France, Airbus A330 Aircraft Characteristics Airport and Maintenance Planning (01 2014).

[41] K. Deb, L. Thiele, M. Laumanns, E. Zitzler, Scalable test problems for evolutionary multi-objective optimization, TIK-Technical Report 112, Institut für Technische Informatik und Kommunikationsnetze, ETH Zürich (2001).

Declaration of interests

☒ The authors declare that they have no known competing financial interests or personal relationships that could have appeared to influence the work reported in this paper.

☐The authors declare the following financial interests/personal relationships which may be considered as potential competing interests:

2020-09-09

Nacelle design for ultra-high bypass ratio engines with CFD based optimisation

Robinson, Matthew

Elsevier

Robinson M, MacManus DG, Christie R, et al., (2020) Nacelle design for ultra-high bypass ratio engines with CFD based optimisation. Aerospace Science and Technology, Volume 113, June 2020, Article number 106191

https://doi.org/10.1016/j.ast.2020.106191